

Comprehensive study of cosmogenic neutron production in large liquid scintillator detectors

Yijian Jiang^a, Jie Cheng^a ^{*}, Haoqi Lu^b [†], and Yaoguang Wang^c

^aSchool of Nuclear Science and Engineering, North China Electric Power University, Beijing 102206, China

^bInstitute of High Energy Physics, Chinese Academy of Sciences, Beijing 100049, China
^cShandong University, Jinan 250100, China

Abstract

Neutrons produced by cosmic ray muons constitute a significant background for underground experiments investigating neutron oscillations, neutrinoless double beta decay, dark matter, and other rare event signals. This work benchmarks measured neutron yields and neutron multiplicities—with a focus on data from the Daya Bay Reactor Neutrino Experiment—against comprehensive simulations using three GEANT4 hadronic physics lists. These simulations are further refined via a TALYS-based adjustment of hadronic cross sections. For the BERT-based models, the adjustment reduces the discrepancy in the total neutron yield from about 20% to approximately 6%, while for the BIC-based models it improves the agreement from roughly 13% to the sub-percent level ($\sim 0.3\%$), indicating a markedly better consistency of the BIC-based models with the experimental data. Nevertheless, a clear tension persists: simulations systematically underproduce single-neutron events while overproducing multi-neutron events. The study establishes a reproducible benchmark for cosmogenic neutron modeling and proposes a targeted refinement strategy—including channel-specific reweighting and intranuclear cascade parameter tuning—to guide future model development.

^{*}Email: chengjie@ncepu.edu.cn

[†]Email: luhq@ihep.ac.cn

1 Introduction

Neutrons produced by cosmic ray muons pose a significant background for large liquid scintillator (LS) detectors in underground experiments, including searches for neutrino oscillations, neutrino-less double beta decay, dark matter, and other rare events. Precise neutron modeling is therefore essential for background suppression and signal identification. Earlier studies, such as that by Wang *et al.* [1], have provided the FLUKA-based predictions for the dependence of the neutron yield on muon energy, with related work also performed by Kudryavtsey *et al.* [2]. Experimental measurements of the neutron yields have been reported by various experiments at different overburden depths. Initial studies at CERN [3] provide fundamental data on neutron production cross-sections. Underground experiments including KamLAND [4], Borexino [5], and Daya Bay [6] have further characterized neutron yields in their respective detector configurations. Additional measurements have been conducted by other groups [7–10, 12, 13]. Beyond total yields, neutron multiplicity distributions—which probe the underlying hadronic dynamics—have been studied at Boulby [13], Borexino [14, 15], Daya Bay [6], and in a different interaction channel by T2K [16].

Despite these experimental efforts, a systematic comparison between measured neutron observables and detailed simulations remains limited. As an example, the Daya Bay [6] have performed a precise measurement of the neutron production rate in LS at three different values of average muon energy with relative systematic uncertainties below 10%. Corresponding predictions are calculated using both FLUKA [17] and GEANT4 [18] simulation tools. However, the simulation results exhibit a discrepancy of $\sim 20\%$ when compared to the measured values. In other experiments, such as KamLAND [4], the discrepancy between simulation and measurement also reaches around 30% or more. Discrepancies persist between default simulation frameworks and experimental data, especially in modeling hadronic interactions relevant for cosmic ray muon interactions. This gap impedes the refinement of simulation tools and constrains background predictions for future experiments, such as the Jiangmen Underground Neutrino Observatory (JUNO) [19].

This work addresses the need for improved simulation accuracy by conducting a comprehensive benchmark study of cosmogenic neutron production in LS detectors, using the Daya Bay experiment as the primary reference. We firstly employ a GEANT4-based simulation approach with three different hadronic physics lists to investigate the impact of hadronic interaction models on neutron production. Furthermore, the simulations are enhanced by a TALYS [20]-based Monte Carlo adjustment scheme, which rescales GEANT4’s inelastic cross sections for incident neutrons, protons, and gamma rays below 200 MeV. This methodology is motivated by the earlier study [21] highlighting limitations in the GEANT4 hadronic models. In particular, the measurements of the reactions between neutron and ^{12}C at CERN have shown that standard GEANT4 physics lists systematically underpredict neutron- ^{12}C reactions. In contrast, the TALYS package with optimized parameters successfully reproduces the measured integral cross section for the $^{12}\text{C}(n, p)^{12}\text{B}$ reaction up to 10 GeV. These findings suggest that TALYS-based adjustments can substantially improve the accuracy of neutron production simulations. A comprehensive simulation study has been performed, covering the characterization of hadronic interaction models, and the estimations of neutron yields and multiplicity distributions. The improvements resulting from the TALYS-based cross section adjustments relative to the GEANT4 physics lists are quantitatively evaluated.

Finally, the simulation results are compared to the Daya Bay measurements [6] to calibrate the hardronic interaction models. Through comparisons between measurements and simulations, this work not only establishes a reproducible benchmark for cosmogenic neutron modeling, but also identifies persistent discrepancies in neutron multiplicity distributions that guide future model development.

The remainder of this paper is structured as follows. Section 2 details the simulation strategy for cosmic muons, covering the cosmic-ray muon flux, the GEANT4-based detector simulation, and the implementation of the TALYS-based hadronic interaction model. Section 3 focuses on the characteristics of cosmogenic neutron production, analyzing relevant inelastic cross sections and the neutron production mechanisms. Section 4 presents the results, comparing simulated and experimental neutron yields and multiplicity distributions. Finally, Sect. 5 summarizes the main findings and provides conclusions.

2 Strategy for simulations

2.1 Cosmic ray muon flux

To compare simulations with experimental data, this work employs measurements from the Daya Bay experiment [6], specifically using its LS detectors positioned in an experimental hall (EH1). This location is both close to the reactor core and situated at a vertical overburden of 250 meters-water-equivalent (m.w.e.). In our simulations, the cosmic ray muon flux has been taken from the Ref. [6] to ensure the muon spectrum accurately represents the experimental conditions. The following is a brief summary of the flux calculation based on Refs. [6, 22].

The muon flux at sea level is well-modeled by Gaisser's formula [23, 24]. For the Daya Bay site, this formula has been modified to better describe the spectrum at low energies and large zenith angles [22], yielding fluxes consistent with previous cosmic ray muon measurements [25–29]. To model site-specific shielding, a digitized mountain profile is generated from local topographic maps. The MUSIC code [30, 31] is then used to propagate muons from the top of this profile, calculating the muon path length through rock. The MUSIC simulation results give a muon rate of 1.27 Hz/m^2 and an average muon energy of 63.9 GeV. Figure 1 shows the muon energy and angular distributions at the EH1. Here, the zenith angle is defined as a muon's angle from the vertical, and the azimuth angle is the compass bearing from true North.

2.2 GEANT4-based detector simulation

GEANT4 is a general-purpose Monte Carlo simulation toolkit developed by CERN, widely used in high-energy and nuclear physics for modeling the passage of particles through matter. It provides a flexible framework to simulate a variety of physical processes, including electromagnetic, hadronic interactions and optical processes, over a broad range of energies. In our simulations, GEANT4 (version 11.2.1) has been employed to model muon-induced neutron production in LS detectors. Unless otherwise noted, all GEANT4 results presented in this work are based on version 11.2.1. For brevity and clarity, the version number will not be repeated in subsequent mentions.

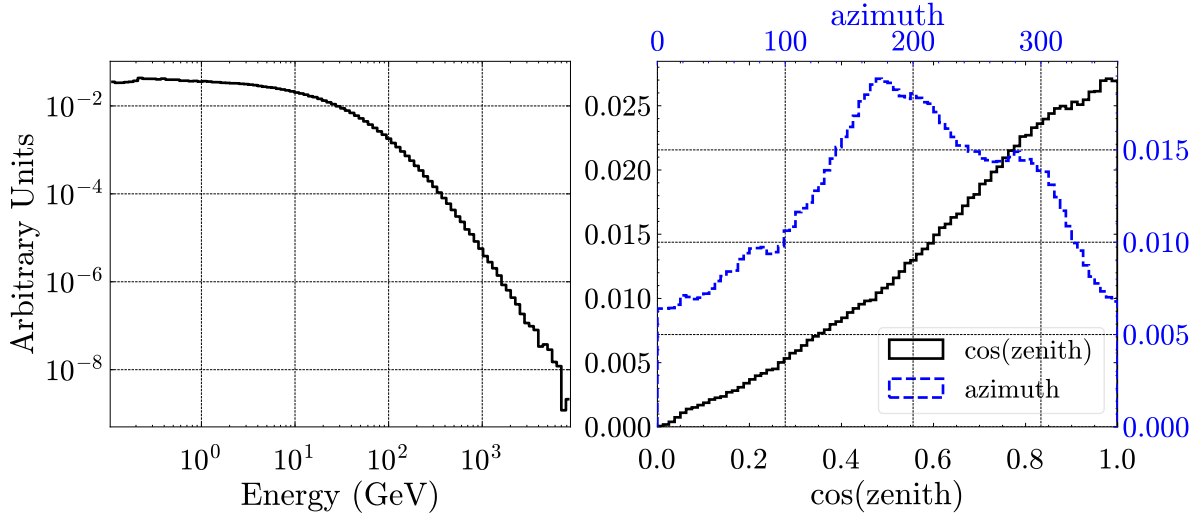


Figure 1: Energy spectrum and the angular distributions of the simulated muons. Left panel: normalized energy spectrum of muons, shown as a probability density with a logarithmic y-axis. Right panel: angular distributions of the muon directions. The black curve shows the probability density as a function of $\cos(\text{zenith})$ (bottom x-axis), while the blue curve shows the azimuth angle distribution (top x-axis). Both angular distributions are normalized to unit area.

A detector geometry is constructed in GEANT4 based on the Daya Bay experimental setup [32]. The detector geometry, illustrated in Fig. 2, comprises three concentric cylindrical regions delineated by transparent acrylic vessels. The central target region (3 m in height and diameter) holds 20 tons of gadolinium-loaded liquid scintillator (GdLS). The material density ($\rho = 0.86 \text{ g/cm}^3$) is adopted from the measured value for the Daya Bay GdLS [33]. This is surrounded by an equal-mass layer of pure LS and an outer mineral oil buffer. The entire assembly is housed within a 5 m \times 5 m stainless steel vessel. The simulation focuses primarily on the GdLS region, where the majority of muon-induced neutrons are both produced and captured. Note that our simulation also includes muon detectors, sever as an water Cherenkov detector, in addition to the primary LS detector setup.

To investigate the model dependence of hadronic interactions, our simulations employ three representative GEANT4 hadronic physics lists: `FTFP_BERT_HP`, `QGSP_BERT_HP`, and `QGSP_BIC_HP`. Figure 3 illustrates the energy-dependent composition of these hadronic physics lists, based on the reference definitions provided in the GEANT4 Physics List Guide [34]. Some comments on the Fig. 3 are helpful.

- In the low- to intermediate-energy regime ($E < 6 \text{ GeV}$), the intranuclear cascade is simulated using either the Bertini (BERT) or Binary (BIC) cascade model. As indicated by the transition regions in Fig. 3, the simulation employs a linear transition in probability between the cascade models and the Fritiof (FTF) string model (typically between 3 and 6 GeV) to ensure continuity in physical observable.
- At higher energies, hadronic interactions are modeled using string excitation and fragmentation frameworks. A key distinction exists between the FTF and QGSP variants. In the `FTFP_BERT_HP` list, the FTF model is used exclusively to handle interactions from the cas-

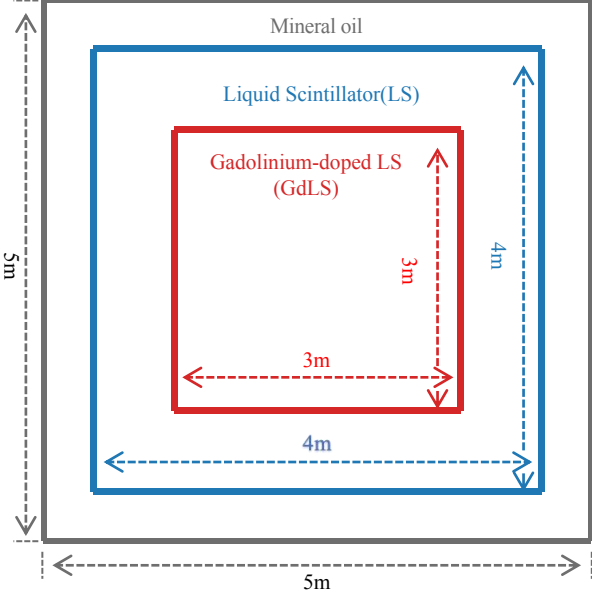


Figure 2: Schematic illustration of the detector geometry used in the simulation, showing the GdLS, LS, and mineral oil regions. The geometry of the water pool surrounding the LS detector is also modeled, though it is not illustrated here.

cade transition region up to the highest energies. Conversely, the QGSP configurations adopt a multi-stage approach: the FTF model serves as an intermediate bridge (typically covering 6-25 GeV) to fill the gap between the cascade regime and the Quark-Gluon String (QGS) model, which dominates at very high energies (> 25 GeV).

- The `QGSP_BIC_HP` configuration utilizes a hybrid scheme in the cascade region: the BIC Cascade model describes the interactions of primary nucleons (p and n), while the BERT model handles other particles, such as pion (π), kaon (K), and γ . This distinction allows for a more detailed treatment of nucleon-induced spallation processes in the intermediate-energy regime.
- All three selected lists incorporate the Neutron High-Precision (HP) package (denoted by the `_HP` suffix). This module utilizes evaluated data-driven cross sections for neutrons below 20 MeV, providing a high-fidelity description of low-energy neutron transport, moderation, and capture processes, which are critical for reproducing thermal-neutron yields in LS detectors.

Note that these physics lists are widely adopted in neutrino and cosmic-ray studies because they provide complementary modeling of hadron-nucleus interactions across different energy ranges. In this work, they are specifically chosen because they span the dominant sources of hardonic interaction model uncertainties in GEANT4: `FTFP_BERT_HP` and `QGSP_BERT_HP` differ in their high-energy string models (FTF vs. QGS), while `QGSP_BIC_HP` replaces the BERT cascade with the BIC Cascade at intermediate energies. Comparing these three lists therefore allows a systematic assessment of both string-model and intranuclear-cascade modeling uncertainties that directly

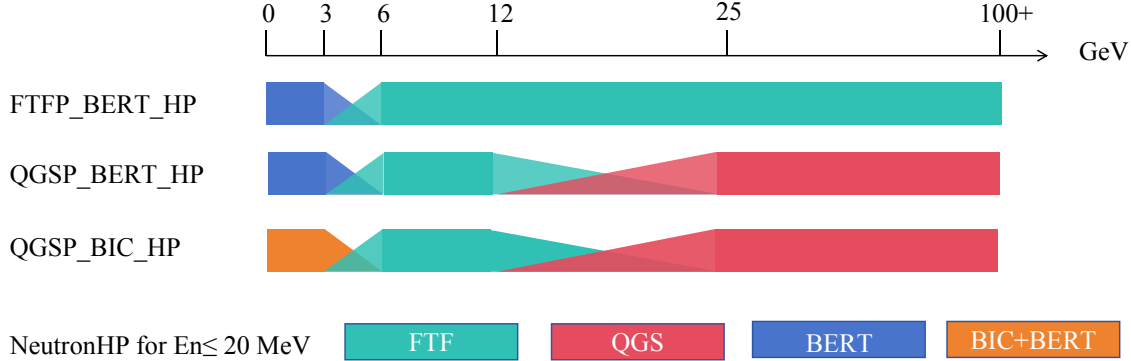


Figure 3: Model composition and energy ranges of the three GEANT4 hadronic physics lists used in this work: **FTFP_BERT_HP**, **QGSP_BERT_HP**, and **QGSP_BIC_HP**. The shaded regions indicate smooth transitions between cascade and string models.

impact the neutron yields.

2.3 TALYS-based hadronic interaction model

The TALYS package [35] models nuclear reactions for projectiles—including p , n , d , t , ${}^3\text{He}$, α , and γ —over energies from 1 keV to 200 MeV. It calculates cross sections, residual nucleus production, and emission spectra using optical, pre-equilibrium, and Hauser–Feshbach statistical models.

This study employs TALYS (1.8) to provide hadronic interaction cross sections for $p-{}^{12}\text{C}$, $n-{}^{12}\text{C}$, and $\gamma-{}^{12}\text{C}$, complementing the GEANT4 simulation. Because TALYS does not simulate $\pi^\pm-{}^{12}\text{C}$ or $\mu-{}^{12}\text{C}$ interactions, these processes are treated exclusively with GEANT4 in this work. Version 1.8 is used to maintain consistency with the TALYS version integral to the TENDL-2017 nuclear data library [36]. TENDL-2017 supplies ENDF-formatted data from default and adjusted TALYS calculations, augmented by other sources. The library and its toolchain have undergone extensive verification, validation, and benchmarking against differential and integral experimental datasets in basic and applied nuclear physics. Another reason for this version choice is that while newer TALYS releases include improvements—notably in photonuclear reactions and fission yields—the optical model parameters and pre-equilibrium descriptions for nucleon-induced inelastic scattering on light nuclei like ${}^{12}\text{C}$ (at energies $E < 200$ MeV) are already well-established in version 1.8. We therefore use TALYS (1.8) as a robust physics baseline to evaluate the inclusive inelastic cross-section discrepancies observed in GEANT4. Note that the TALYS (1.8) is used throughout this work. Subsequent references to TALYS will omit the version number for clarity.

To incorporate the TALYS-based hadronic cross sections into the GEANT4 simulations, we have noted that a single μ -induced cascade comprises multiple individual n -producing vertices. Consequently, we implement a vertex-level reweighting scheme for each μ event. In this TALYS-based MC framework, the total neutron number for a μ event, denoted N_n^T , is calculated as per Eq. 2.1 by reweighting each new n generated vertex i according to the parent particle type j (for $j = n, p, \gamma$) and its kinetic energy E_i .

$$N_n^T = \sum_{i,j} N_{i,j}^G \times W_{i,j}(E_i, j) \quad (2.1)$$

where $N_{i,j}^G$ denotes the number of neutrons produced at vertex i by a parent particle of type j (for $j = n, p, \gamma$) in the original GEANT4 simulation. The corresponding weighting factor $W_{i,j}$ is derived from the exclusive new- n -generation inelastic cross sections (σ_{in}) and is defined as:

$$W_{i,j} = \begin{cases} \frac{\sigma_{in,j}^T(E_i)}{\sigma_{in,j}^G(E_i)} & \text{for } j = n, p, \gamma \text{ on } {}^{12}\text{C} \\ 1 & \text{otherwise} \end{cases} \quad (2.2)$$

Where, σ_{in}^G and σ_{in}^T denote the GEANT4 and TALYS exclusive inelastic cross sections for new n generated reactions, respectively. Note that for vertices with $E_i > 200$ MeV (beyond TALYS's range), we set $W_{i,j} = 1$, using the original GEANT4 result. What's more, if an exclusive new- n -generation channel predicted by the original GEANT4 simulation is absent from TALYS, its corresponding $W_{i,j}$ is set to 1, leaving its cross section unchanged.

This reweighting scheme adjusts the interaction rate for exclusive channels (governed by their exclusive σ_{in}) while preserving the final-state multiplicity and kinematics predicted by GEANT4. Crucially, it does not substitute GEANT4's exclusive channels—which rely on its internal de-excitation models (e.g., Fermi break-up)—with TALYS predictions event by event. Such a substitution would violate the kinematic consistency of the simulated cascade, as secondary particle momenta must be balanced with the specific nuclear remnant. Instead, our hybrid method renormalizes the reaction probability using more accurate nuclear data from TALYS.

3 Characteristics of cosmogenic neutron production

In our GEANT4-based detector simulations, cosmic muons have been sampled above the detector geometry (Fig. 2), following the energy and angular distributions shown in Fig. 1. The propagation of these muons through the full detector geometry has simulated using three representative GEANT4 hadronic physics lists: `FTFP_BERT_HP`, `QGSP_BERT_HP`, and `QGSP_BIC_HP`, as detailed in Sect. 2. The neutron yield is defined as the number of neutrons produced per incident muon, per unit path length, and per unit material density. To enable a direct comparison with Daya Bay measurements [6]—specifically those involving GdLS—our simulation focuses on muons traversing the GdLS region. This corresponds to the experimental procedure where neutrons captured on Gd, following an identified muon in the LS, are selected. Consequently, we have analyzed the corresponding muon tracks through GdLS and the subsequent neutron production within this volume.

Simulation results show that $\sim 61\%$ of muons depositing at least 20 MeV in the LS also traverse the GdLS. This fraction is consistent across the three physics lists and agrees with Daya Bay simulations [6]. Furthermore, the average muon path length in the GdLS (L_{avg}), a geometry-dependent parameter sensitive to the muon angular distribution, is about 206.3 cm for EH1 in our simulations. This value is also consistent across physics lists and compares well with the 204.1 cm obtained from Daya Bay simulations for EH1 [6]. Finally, we have verified the distribution

of energy deposited in the LS by muons with a nonzero track length in the LS against Daya Bay measurement data [6]; the spectral shapes are consistent between our simulations and the experimental data.

The following part of this section analyzes the characteristics of the resulting neutron production processes. First, we compare inelastic reaction cross sections for neutron production in the GdLS region. Then, this analysis progresses from energy-dependent inelastic cross section predictions to an examination of dominant neutron multiplying reaction channels. Finally, exclusive cross sections are evaluated to quantify the model-dependent differences that directly impact for spallation neutron modeling.

3.1 Inelastic cross sections

The dominant contributors to μ -induced neutron production in GdLS region are secondary n , p , γ , π^+ , and π^- . These particles, generated primarily along muon tracks through electromagnetic and hadronic cascades, initiate the subsequent interactions with carbon nuclei that yield spallation neutrons. Therefore, a detailed characterization of the inelastic reaction cross sections (σ_{in}), for these projectiles interacting with ^{12}C is essential for identifying the microscopic origins of spallation neutron and benchmarking model-dependent effects.

The inclusive σ_{in} is a fundamental quantity governing the neutron production rate. To investigate model dependencies, the σ_{in} for the TALYS-supported projectiles, namely n , p , and γ , incident on ^{12}C using TALYS, is compared to the predictions of three GEANT4 hadronic physics lists: `FTFP_BERT_HP`, `QGSP_BERT_HP`, and `QGSP_BIC_HP`. Because TALYS cannot model π^\pm or μ^\pm as projectiles, the TALYS-GEANT4 comparison is performed only for the n , p , and γ channels, whereas the π^\pm (and μ^\pm) contributions are included solely in the full GEANT4-based evaluation of μ -induced neutron production. Since the incident energy simulated by TALYS is limited to 200 MeV, Fig. 4 presents the comparison across this energy range. For the comparison of these GEANT4 physical model lists, we have found that the inclusive σ_{in} across the full energy range for these particles are nearly identical. This consistency can be understood as follows.

- For p and γ , the hadronic models BERT and BIC are used for $E < 200$ MeV. Consequently, the cross sections from `FTFP_BERT_HP` and `QGSP_BERT_HP` are identical.
- For n , the HP model is applied below 20 MeV, while above this threshold the same BERT/BIC models used for p and γ are employed. Therefore, below 20 MeV the cross sections from all three lists coincide, whereas above 20 MeV the results from `FTFP_BERT_HP` and `QGSP_BERT_HP` are the same.
- The inclusive cross sections for n , p , and γ from the BERT and BIC models are themselves very similar in this energy range. However, significant differences emerge in exclusive reaction channels, as will be shown in Fig. 5.

Turning to the comparison between TALYS and GEANT4, the inclusive σ_{in} for n and p from TALYS and GEANT4 exhibit agreement in the spectral shape in Fig. 4, but a systematic discrepancy in magnitude: TALYS values are $\sim 20\%$ (n) and 30% (p) higher across this energy

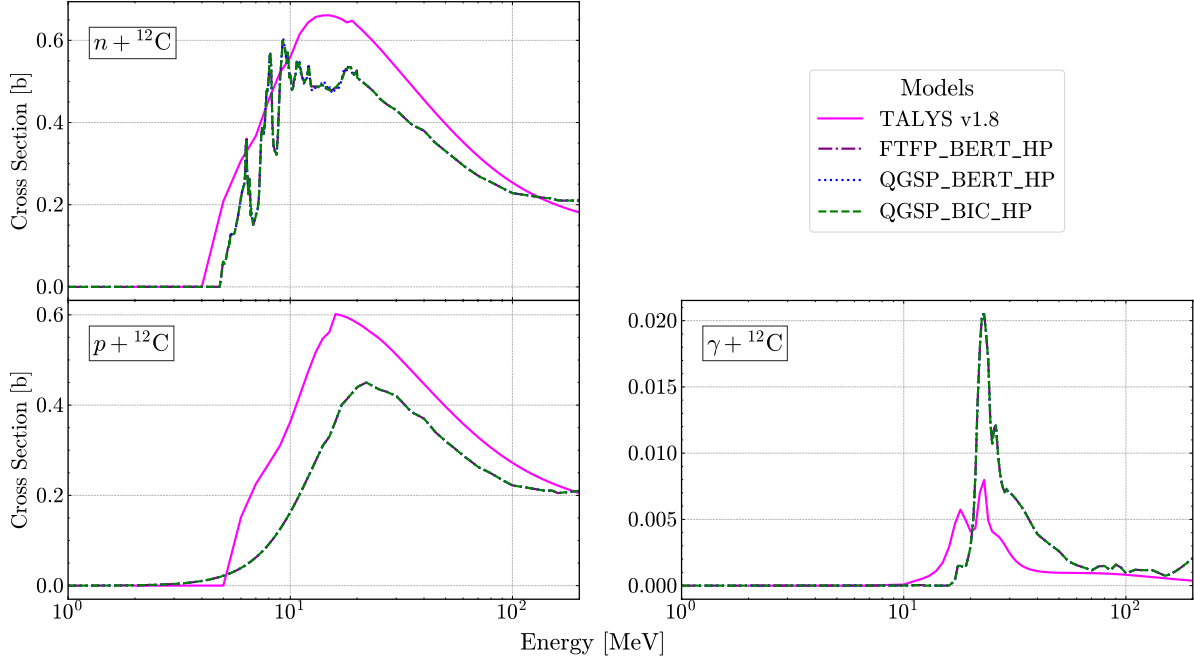


Figure 4: Comparison of inclusive inelastic cross sections ($\sigma_{in}(E)$) for n , p , and γ interacting with ^{12}C , obtained from TALYS and GEANT4 hadronic models (FTFP_BERT_HP, QGSP_BERT_HP, and QGSP_BIC_HP). Note that charged pions are not included in this comparison as they are not supported by the TALYS framework.

range. For γ , notable differences emerge: the TALYS cross section peak is shifted to lower energies and its overall magnitude is roughly 50% lower than that of GEANT4.

Given our focus on exclusive channels related to neutron generation, we have analyzed the exclusive cross sections of the dominant new-neutron-producing channels, where the final-state neutron count exceeds that of the incident particles. A previous study [37] has calculated exclusive cross sections for n -induced reactions on ^{12}C using TALYS, identifying $^{12}\text{C}(n, 2n)^{11}\text{C}$ and $^{12}\text{C}(n, 2n\alpha)^7\text{Be}$ as the dominant new-neutron-generation channels. Following this work, we have performed analogous TALYS calculations for p - and γ -induced reactions on ^{12}C . For $p-^{12}\text{C}$ reactions, the dominant new-neutron-generation channels are $^{12}\text{C}(p, n)^{12}\text{B}$ and $^{12}\text{C}(p, np)^{11}\text{C}$. For $\gamma-^{12}\text{C}$ reactions, the dominant channel is $^{12}\text{C}(\gamma, 2n2p)^8\text{Be}$.

The exclusive cross sections for n -, p -, and γ -induced reactions on ^{12}C are also obtained from GEANT4. Fig. 5 shows the energy dependence of these leading channels, selected from the highest-probability modes in the GEANT4 FTFP_BERT_HP physics list. Each panel, corresponding to a different projectile (n , p , or γ), compares the predictions of three GEANT4 physics lists with the available TALYS calculations. For the $^{12}\text{C}(n, 2n)^{11}\text{C}$ and $^{12}\text{C}(p, pn)^{11}\text{C}$ channels, the cross sections predicted by FTFP_BERT_HP and QGSP_BERT_HP are essentially identical across the 0–200 MeV. This indicates that, the BERT intra-nuclear cascade is dominant in this energy range. The choice of high-energy string model (FTF vs. QGS) has little impact on these particular channels. In contrast, QGSP_BIC_HP, which substitutes BIC for BERT at intermediate energies, yields significantly different cross sections, particularly in the tens-of-MeV region. This result demonstrates that within GEANT4, the treatment of the intra-nuclear cascade is more influential

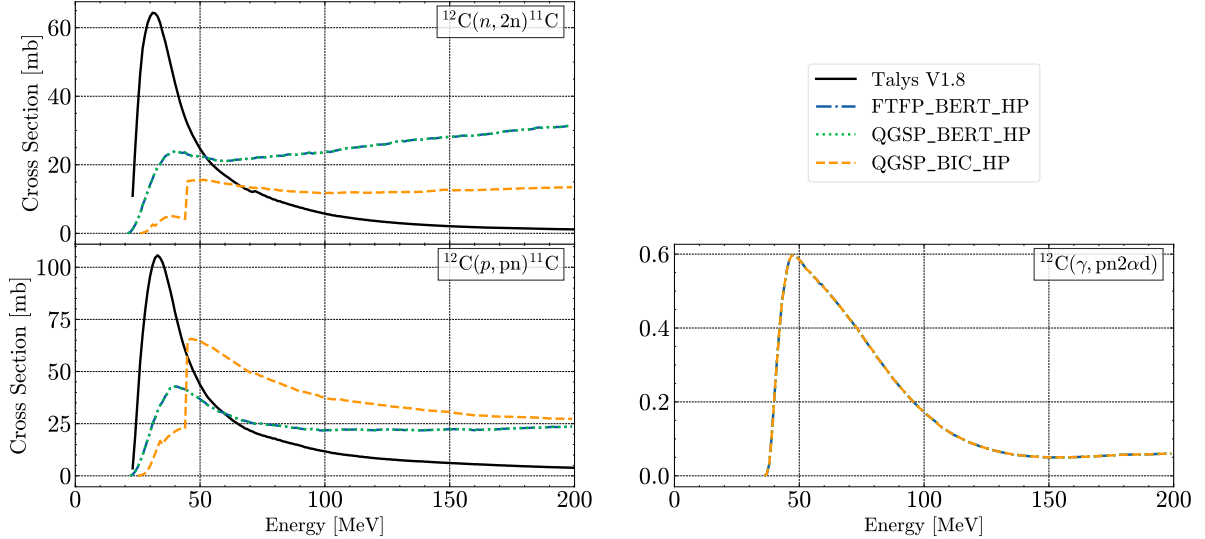


Figure 5: Comparison of the dominant neutron-multiplying inelastic reaction-channel cross sections for n , p , and γ projectiles on ^{12}C below 200 MeV. For each projectile, the reaction channel in which the total n number in the final state exceeds that of the incident particle and has the highest occurrence probability in GEANT4 FTFP_BERT_HP is identified, and the corresponding cross sections are compared with those from QGSP_BERT_HP, QGSP_BIC_HP, and TALYS.

than the string model in determining the relative weights of specific n -producing channels. In the QGSP_BIC_HP physics list, the BERT model remains active for projectiles other than neutrons and protons. Therefore, the exclusive cross sections for γ -induced neutron production are the same across all three physics lists.

When compared to TALYS, systematic differences become apparent. For the n - and p -induced neutron examples, TALYS predicts a pronounced maximum near threshold and generally larger inelastic strengths at low energies for the $^{12}\text{C}(n, 2n)^{11}\text{C}$ and $^{12}\text{C}(p, pn)^{11}\text{C}$ channels than any of the three GEANT4 physics lists. For the γ -induced neutron case, GEANT4 identifies a highly specific multi-fragment breakup channel, $^{12}\text{C}(\gamma, pn2ad)$, as the most probable neutron-multiplying mode in FTFP_BERT_HP, and all three physics lists yield almost identical cross sections for this channel. TALYS, however, assigns negligible strength to this exclusive high-multiplicity final state within its Hauser–Feshbach framework. The presence of this channel in GEANT4 and its practical absence in TALYS further highlights the differences in the deexcitation modeling of highly excited ^{12}C between the two simulation tools.

Collectively, Figs. 4–5 reveal that although GEANT4 physics lists are self-consistent and reproduce the qualitative trends of dominant neutron-production channels, they underestimate low-energy inelastic strength relative to TALYS. The more detailed nuclear-structure and energy-dependence effects in TALYS motivate the hybrid rescaling scheme (Sec. 2.3) developed to improve simulations of μ -induced spallation neutrons.

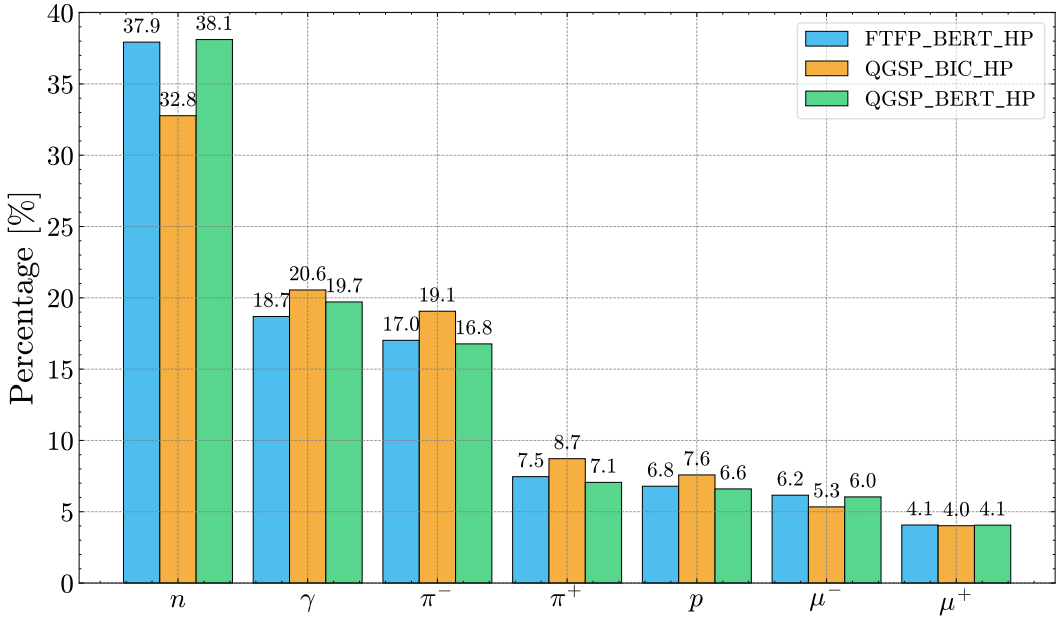


Figure 6: Distribution of parent particles responsible for neutron production under different hadronic physics lists. The relative contributions (%) of each parent type are compared among FTFP_BERT_HP, QGSP_BERT_HP, and QGSP_BIC_HP.

3.2 Production of cosmogenic neutrons

Following the GEANT4-based simulation of cosmic muons, we have investigated the neutron-producing processes to quantify the impact of different hadronic models on secondary neutron generation. We isolate channels resulting in net neutron gain (final-state neutrons > incident neutrons). For inelastic interactions on ^{12}C , the fraction of events leading to new neutron neutron generation varies by projectile and GEANT4 physics list.

For the new-neutron-producing processes, Fig. 6 presents the relative contributions of various parent particles to the new neutron production across the three GEANT4 physics lists. The results reveal that n -, γ -, and π^- -induced reactions dominate the overall neutron yield, followed by processes induced by π^+ , protons, and muons. Comparison of the physics lists reveals a distinct behavior for QGSP_BIC_HP. While the two BERT-based models (FTFP_BERT_HP and QGSP_BERT_HP) exhibit nearly identical distributions, QGSP_BIC_HP predicts a **lower** relative contribution from n -induced reactions ($\sim 32.8\%$ vs. $\sim 37.9\%$) and an **enhanced** contribution from charged pions and protons. This shift is consistent with the model definitions: QGSP_BIC_HP employs the BIC model for nucleons (n, p) but retains the BERT model for other particles. The difference suggests that the BIC treatment of nucleon-nucleus interactions alters the branching ratios of secondary cascades, effectively redistributing the production weight toward π^- - and p -mediated channels relative to the BERT model.

Next, we have examined the kinetic-energy distributions of the parent particles at the neutron-production vertex. Figure 7 compares the channel-resolved parent-energy spectra across the three physics lists. For all initiating particles (n, p, γ and π^\pm), the spectra feature a prominent soft component below ~ 150 MeV and a long high-energy tail extending up to the GeV scale. Hadronic parents p (and, similarly, π^\pm) tend to exhibit somewhat harder high-energy tails than γ and n ,

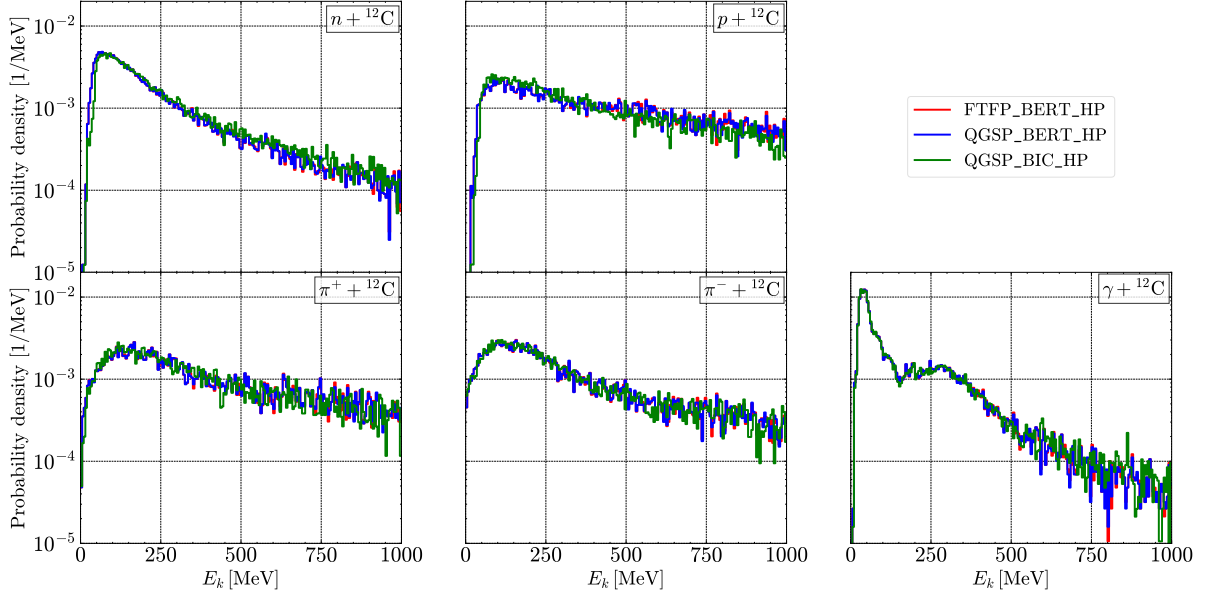


Figure 7: Parent-particle kinetic-energy spectra at the neutron-production vertex, resolved by initiating particle ($n \rightarrow n$, $p \rightarrow n$, $\gamma \rightarrow n$ and $\pi^\pm \rightarrow n$) for three GEANT4 physics lists.

consistent with intranuclear-cascade kinematics and multi-nucleon emission in spallation reactions. The remarkable stability of these spectral shapes among the physics lists suggests that the variations in the relative contributions of parent particles for neutron productions (Fig. 6) are driven primarily by differences in **reaction probabilities (cross sections) and branching ratios**, rather than by large shifts in the accessible kinetic-energy phase space of the parent particles.

Complementing the inclusive reaction comparisons for individual parent particles in Figs. 6,7, we investigate how GEANT4 hadronic models distribute reaction strength across specific neutron-producing channels. Fig. 8 displays the relative final-state neutron multiplicity distributions from new-neutron-generation interactions on a ^{12}C target, categorized by parent-particle types, such as $n, p, \pi^+, \pi^-, \mu^+, \mu^-$, and γ . For n -induced interactions, event fractions with exactly 2, 3, 4, and >4 new neutrons are normalized to 100%. For all other parent particles, fractions for exactly 1, 2, 3, and >3 new neutrons are similarly normalized to 100%. Discrepancies in dominant neutron-generation channels between BERT and BIC physics lists for $n-^{12}\text{C}$ and $p-^{12}\text{C}$ show that BIC favors final states with higher neutron multiplicity. This is evident in Fig. 8, where differing channel weights across models lead to variations in predicted neutron yields. A direct comparison for γ, π^\pm and μ^\pm projectiles is not possible, as the BIC model is not applicable to these interactions on ^{12}C .

4 Benchmarking simulations against experimental data

A key observable for calibrating the hadronic interaction models is the neutron yield, Y_n . Following the definition in Ref. [6], it is given by

$$Y_n = \frac{N_n}{N_\mu L_{\text{avg}} \rho}, \quad (4.3)$$

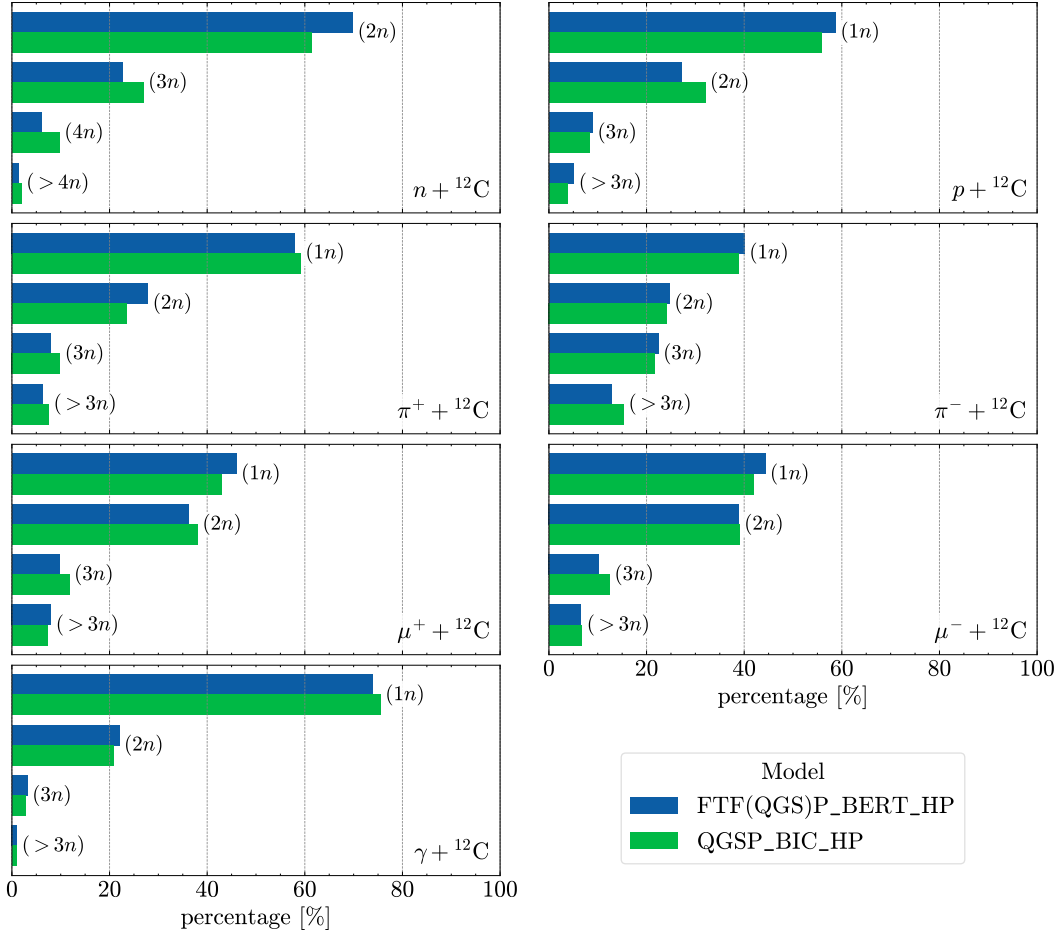


Figure 8: Distributions of exclusive new-neutron-generation reactions on ^{12}C for various parent particles ($n, p, \pi^+, \pi^-, \mu^+, \mu^-, \gamma$), categorized by the associated final state neutron multiplicities. Events are required to have at least one newly produced neutron. For n -induced interactions, event fractions with exactly 2, 3, 4, and >4 new neutrons are shown, normalized to 100%. For all other parent particles categories, fractions are shown for exactly 1, 2, 3, and >3 new neutrons, also normalized to 100%. Blue histograms represent the nearly identical results from the GEANT4 physics lists FTFP_BERT_HP and QGSP_BERT_HP, while green histograms show the results from QGSP_BIC_HP for comparison.

where N_n is the number of neutrons produced in association with N_μ muons traversing the GdLS target, while L_{avg} and ρ are the average muon path length and the material density, respectively, whose values have been presented in Sects. 3 and 2. A second key observable is the tagged neutron multiplicity, defined as the number of neutrons captured on Gd following a muon with a nonzero track length in the LS region. This observable is directly comparable with the Daya Bay results [6] and reflects the complexity of μ -induced spallation cascades. The remainder of this section presents the data–simulation comparison for both observables.

As shown in Sect. 3, the physics lists FTFP_BERT_HP and QGSP_BERT_HP yield statistically identical results for all observables in this work. This agreement is expected, as both employ the same BERT intranuclear cascade model for low- and intermediate-energy hadron transport in the μ -induced spallation regime. To simplify the presentation and focus the comparison on the

impact of the intranuclear cascade model, we therefore adopt FTFP_BERT_HP as the representative BERT-based list in subsequent figures. Consequently, the data–simulation comparisons in this section are presented only for FTFP_BERT_HP and QGSP_BIC_HP.

4.1 Neutron yield

According to Eq. 4.3, we calculate the neutron yield, Y_n^G , for each GEANT4 physics list. In this work, the original simulation yield Y_n^G is obtained directly from the GEANT4 output. The TALYS-based MC yield, Y_n^T , is evaluated using the same definition but with the raw GEANT4 neutron count N_n replaced by the corrected count obtained from the event-by-event reweighting scheme detailed in Sect. 2.3.

The calculated neutron yields are summarized in Tab. 1. In the original GEANT4 simulations, the FTFP_BERT_HP physics list yields a neutron yield of about $12.3 \times 10^{-5} \mu^{-1} \text{g}^{-1} \text{cm}^2$, while QGSP_BIC_HP gives a slightly lower value of $11.9 \times 10^{-5} \mu^{-1} \text{g}^{-1} \text{cm}^2$. Compared to the Daya Bay measurement of $10.26 \times 10^{-5} \mu^{-1} \text{g}^{-1} \text{cm}^2$ [6], both original GEANT4 lists overestimate the yield by roughly 13%–20%. The application of the TALYS-based reweighting results in a systematic reduction of the neutron yield for both physics lists. As shown in Tab. 1, the corrected (TALYS-based) yields are 12–14% lower than the original GEANT4 predictions. This adjustment leads to a substantially improved agreement with the experimental measurement. Specifically, for FTFP_BERT_HP, the deviation from the Daya Bay result is reduced from approximately +20% to about +6%. For QGSP_BIC_HP, the original overprediction of roughly +13% is reduced to a level essentially consistent with the data, yielding a residual ratio of $R_{\text{T/D}} = \frac{Y_n^T - Y_n^D}{Y_n^D} \times 100\% \approx -0.39\%$.

Table 1: Comparison of simulated neutron yields with the Daya Bay measurement. Y_n^G denotes the neutron yield from the original GEANT4 physics lists, and Y_n^T stand for the modified yield based on TALYS hadronic cross sections. For reference, the measured neutron yield is $Y_n^D = (10.26 \pm 0.86) \times 10^{-5} \mu^{-1} \text{g}^{-1} \text{cm}^2$, which is the neutron yield obtained from the Daya Bay experiment in EH1 [6]. The relative differences with respect to data are defined as $R_{\text{G/D}} = \frac{Y_n^G - Y_n^D}{Y_n^D} \times 100\%$ and $R_{\text{T/D}} = \frac{Y_n^T - Y_n^D}{Y_n^D} \times 100\%$.

Physics List	Y_n^G ($\times 10^{-5} \mu^{-1} \text{g}^{-1} \text{cm}^2$)	Y_n^T ($\times 10^{-5} \mu^{-1} \text{g}^{-1} \text{cm}^2$)	$R_{\text{G/D}}$	$R_{\text{T/D}}$
FTFP_BERT_HP	12.31	10.88	+20.0%	+6.04%
QGSP_BIC_HP	11.88	10.22	+13.0%	-0.39%

The significant reduction from Y_n^G to Y_n^T demonstrates the sensitivity of the total neutron yield to inelastic cross sections in the intermediate energy range (50–200 MeV). This shift can be understood by examining the differences between TALYS and GEANT4 for the dominant new-neutron-generation channels between TALYS and GEANT4, as illustrated in Fig. 4. While TALYS predicts higher cross sections at specific low energies, its values are systematically lower than GEANT4’s across the broad 50–200 MeV region, where a substantial portion of the secondary cascade flux resides. Consequently, incorporating the more accurate TALYS nuclear re-

Table 2: Comparison of the number of neutrons produced along muon tracks within the GdLS (N_{gen}), the number of neutrons captured on Gd, for muons with a nonzero track length in LS (N_{nGd}), and the corresponding capture efficiency (ξ_{cap}) for the GEANT4 hadronic physics lists.

Physics List	N_{gen}	N_{nGd}	ξ_{cap}
FTFP_BERT_HP	27,830	18,710	0.67
QGSP_BIC_HP	26,227	18,219	0.69

action probabilities provides a physics-driven correction that effectively counteracts GEANT4’s overprediction. However, it is important to note that the hadronic interaction cross sections provided by TALYS are limited to energies up to 200 MeV and therefore do not extend to the higher-energy regime responsible for the spallation neutron production.

4.2 Tagged neutron multiplicity

Following cosmogenic neutron production in the GdLS region, most neutrons undergo capture on Gd, producing an 8 MeV gamma-ray cascade. The Daya Bay analysis [6] determines the μ -induced neutron yield by selecting neutron captures on Gd that follow a tagged muon signal. In our simulations, we perform three corresponding quantitative evaluations:

1. **Generated neutrons** (N_{gen}): number of neutrons produced along μ tracks within the GdLS.
2. **Captured neutrons** (N_{nGd}): number of neutrons that capture on Gd, for muons with a nonzero track length in the LS region (see Fig. 2).
3. **Capture fraction** (ξ_{cap}): corresponding capture efficiency, defined as $\xi_{\text{cap}} = N_{\text{nGd}}/N_{\text{gen}}$.

Table. 2 summarizes these three key observables for GEANT4 FTFP_BERT_HP, and QGSP_BIC_HP hadronic physics lists. The capture efficiency exhibits a narrow spread, ranging from 0.67 to 0.69 across these physics lists. This consistency indicates that, conditional on neutron production, the capture probability is governed primarily by factors common to all simulations: the detector geometry, the Gd-doping concentration, and the low-energy neutron transport and capture physics. These common components—specifically, the HP neutron scattering model below ~ 20 MeV and the neutron-capture physics implemented via `G4NeutronRadCapture` and `G4NeutronCaptureXS`—are shared identically across the physics lists [34].

The tagged neutron multiplicity (N_{multi}) for a muon passing through the LS region is extracted directly from the original GEANT4 simulation, denoted as $N_{\text{multi}}^{\text{G}}$. For the TALYS-based MC, it is computed in two steps. First, the adjusted number of generated neutrons (N_n^{T}) for a muon passing through the LS region is calculated using Eq. 2.1. The corresponding tagged neutron multiplicity, $N_{\text{multi}}^{\text{T}}$, is then obtained by applying the event-specific capture fraction ξ_{cap} derived from the GEANT4 simulation:

$$N_{\text{multi}}^{\text{T}} = N_n^{\text{T}} \times \xi_{\text{cap}}. \quad (4.4)$$

This approach relies on the assumption that, for a given muon event, the capture fraction is determined predominantly by the overall event topology and detector geometry, and is largely

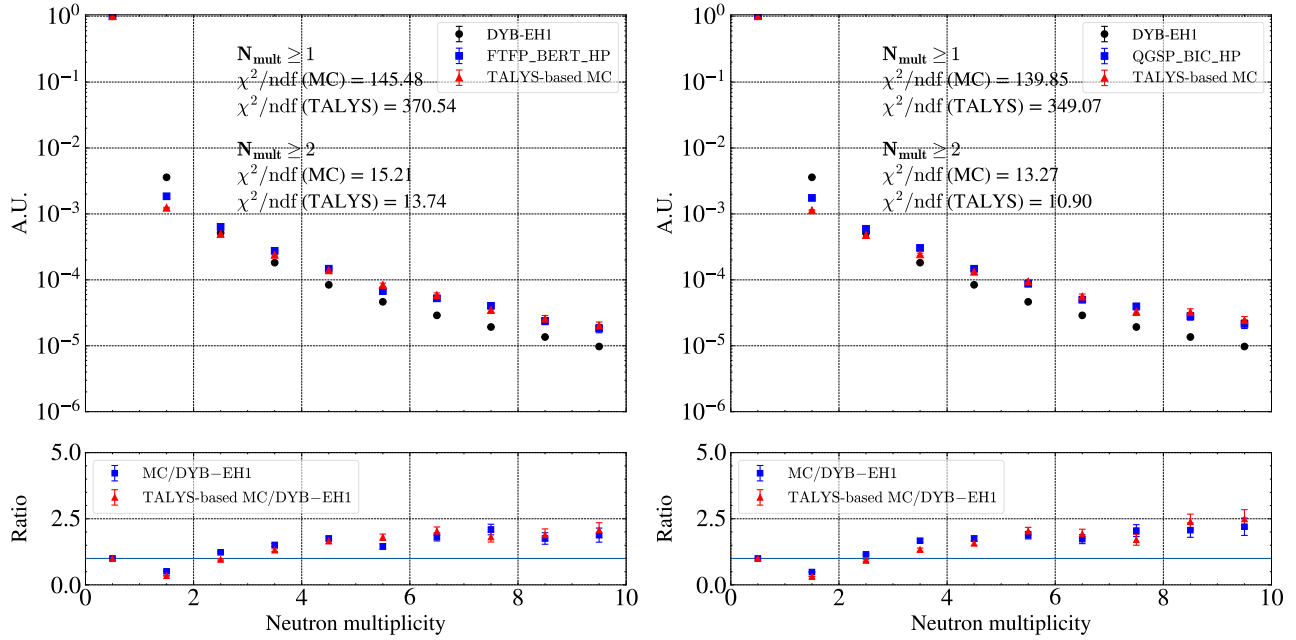


Figure 9: Comparison of the tagged neutron multiplicity distributions between the Daya Bay measurement [6] and simulations. The left (right) panel shows the results for the FTFP_BERT_HP (QGSP_BIC_HP) physics list. In the upper sub-panels, the experimental data from the EH1 LS detector (DYB-EH1) (black markers) are compared with predictions from the original GEANT4 simulation (blue markers) and the TALYS-based MC (red markers). All spectra are normalized to unit area (A.U.), and the error bars represent statistical uncertainties propagated from Poisson counting. Only neutron multiplicities up to $N_{\text{multi}} = 10$ are shown, as the contribution from higher-multiplicity events is negligible. The lower sub-panels present the bin-by-bin ratios of MC to data. The χ^2/ndf values displayed in the upper panels are computed as $\chi^2 = \sum_i (D_i - M_i)^2 / (\sigma_{D,i}^2 + \sigma_{M,i}^2)$ using bins with non-zero contents, and are quoted for $N_{\text{multi}} \geq 1$ and for $N_{\text{multi}} \geq 2$.

insensitive to the reweighting of individual vertices. This is an excellent approximation for our setup, as evidenced by the stability of ξ_{cap} across physics lists, as shown in Tab. 2.

The top panels of Fig. 9 show the tagged neutron multiplicity distributions from the original GEANT4 simulation and the TALYS-based MC, for the FTFP_BERT_HP and QGSP_BIC_HP physics lists, respectively. To compare with the experimental data, the data from the Daya Bay EH1 LS detector (DYB-EH1) [6] is also presented in the top panels of Fig. 9. All spectra are normalized to unit area, and the error bars represent statistical uncertainties only. Note that in Ref. [6], the comparison of neutron multiplicity between the data and MC in EH1 has been performed. For this comparison, the GEANT4 (version 9.2p01) is used. It is found that the difference is largest when neutron multiplicity equals 1, which is the most dominant neutron multiplicity for cosmogenic neutron production. In this work, similar comparisons have been performed in Fig. 9. The bottom panels of Fig. 9 show the ratios of the simulation results to the experimental data. For left and right panels, two ratios are presented: the original GEANT4 prediction to data (MC/DYB-EH1) and the TALYS-based adjusted prediction to data (TALYS-based MC/DYB-EH1). To further assess the consistency between data and simulations with different hadronic models, we quantify the goodness-of-fit using a bin-by-bin χ^2 test that incorporates statistical

uncertainties. The χ^2 is calculated using bins with non-zero content according to

$$\chi^2 = \sum_i \frac{(D_i - M_i)^2}{\sigma_{D,i}^2 + \sigma_{M,i}^2}, \quad (4.5)$$

where D_i and M_i denote the content of the i -th bin for the data and the simulation, respectively, and $\sigma_{D,i}$ and $\sigma_{M,i}$ are their corresponding statistical uncertainties. The goodness of fit is quantified by the χ^2 per degree of freedom (χ^2/ndf). Values are reported separately for two event selections: those with neutron multiplicity $N_{\text{multi}} \geq 1$ and those with $N_{\text{multi}} \geq 2$. For each selection, we quote χ^2/ndf for the original GEANT4 simulation (denoted $\chi^2/\text{ndf}(\text{MC})$) and for the TALYS-based MC prediction (denoted $\chi^2/\text{ndf}(\text{TALYS})$). Key observations from Fig. 9 are summarized as follows.

- **Neutron multiplicity** $N_{\text{multi}} = 1$: All simulation predictions underestimate the experimental data. Applying the TALYS-based correction further enlarges this discrepancy for both physics lists. This is reflected in the χ^2/ndf values: for events with $N_{\text{multi}} \geq 1$, the χ^2/ndf from the TALYS-based MC is worse than that from the original GEANT4 prediction.
- **Neutron multiplicities** $N_{\text{multi}} > 1$: While all simulations systematically overestimate the data in this region, the TALYS-based MC spectra show slightly better agreement. The improvement is most pronounced in the multiplicity range ($N_{\text{multi}} = 2\text{--}8$), where the original GEANT4 predictions exhibit a marked tendency to overproduce multi-neutron events.
- **Comparison of hadronic models**: For all multiplicities, the original GEANT4 prediction using the BIC-based model agrees better with data than the prediction using the BERT-based model. The corresponding TALYS-based MC corrections preserve this relative behavior. This conclusion is also supported by the comparison of the neutron yield.

To investigate the composition of events with $N_{\text{multi}} = 1$ and $N_{\text{multi}} > 1$ in detail, Fig. 10 presents the relative contributions of various parent particles to these event classes. We compare the original GEANT4 physics lists (FTFP_BERT_HP and QGSP_BIC_HP) with their TALYS-based counterparts. The results indicate that single-tagged-neutron events are predominantly induced by $\gamma-^{12}\text{C}$ and $n-^{12}\text{C}$ reactions, whereas multi-tagged-neutron events primarily originate from secondary neutron interactions. A comparison between the physics lists shows that QGSP_BIC_HP predicts a higher fraction of γ -induced single-tagged-neutron events and a slightly lower fraction of n -induced multi-tagged-neutron events relative to FTFP_BERT_HP.

Given the superior agreement of the original BIC-based GEANT4 model with the data across all multiplicities compared to the BERT-based model, a promising strategy for reducing the remaining data–MC discrepancy is to adjust the key inelastic cross sections. Specifically, this would involve increasing the $\gamma-^{12}\text{C}$ cross section for single-tagged-neutron events. This direction is partially validated by the application of TALYS-based hadronic cross sections. In the TALYS-based MC, the fraction of $\gamma-^{12}\text{C}$ reactions contributing to events with $N_{\text{multi}} = 1$ is lower than in the original GEANT4 simulation, which worsens the agreement with data for this channel.

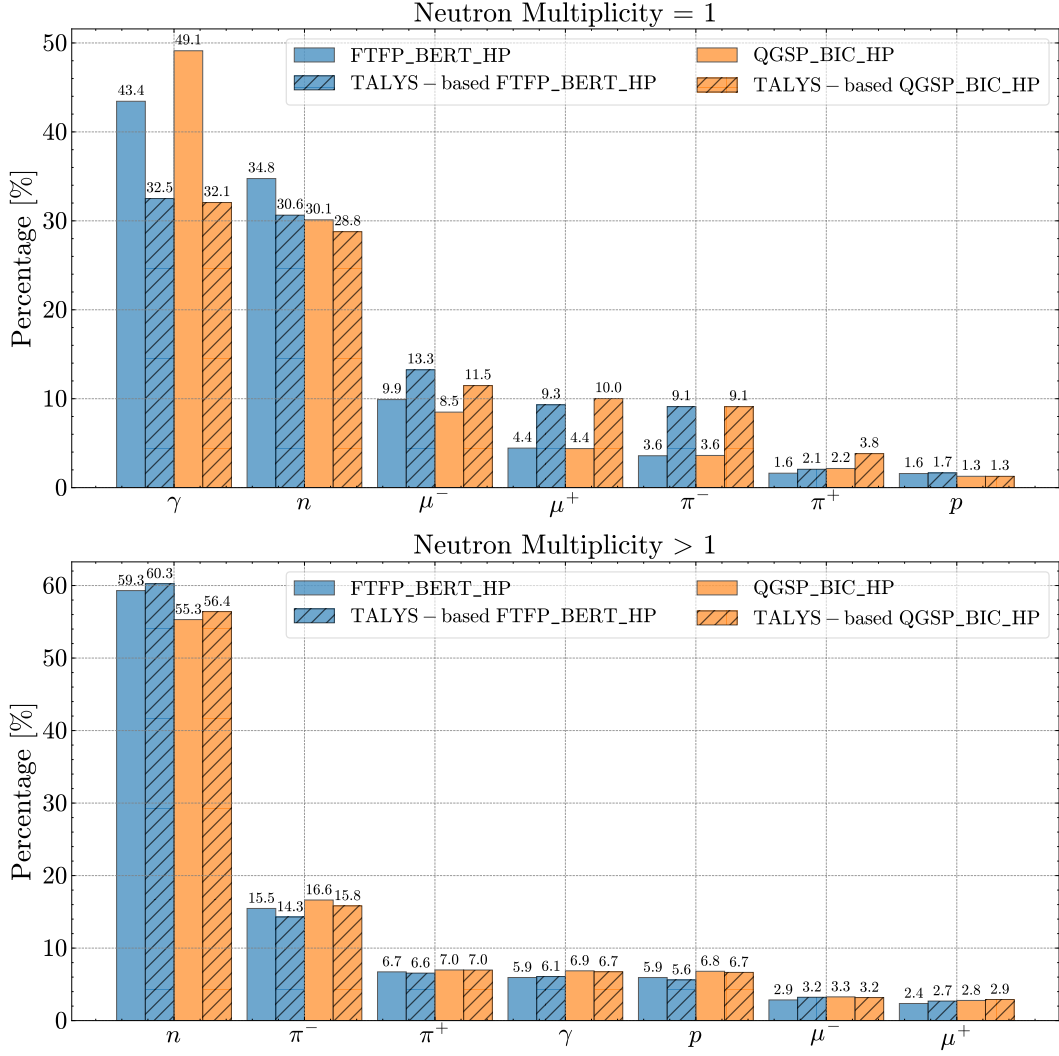


Figure 10: Parent particle contributions to neutron-producing events for the original GEANT4 physics lists FTFP_BERT_HP, QGSP_BIC_HP and their TALYS-based MC variants. The upper panel shows events with exactly one tagged neutron ($N_{\text{multi}} = 1$), while the lower panel corresponds to events with multiple tagged neutrons ($N_{\text{multi}} > 1$). For each parent species (γ , n , μ^\pm , π^\pm , p), the relative fractions are compared side by side, illustrating the redistribution of contributions in the TALYS-based MC.

5 Summary

This work presents a benchmark study of cosmogenic neutron production in large LS detectors. We perform detailed simulations based on the Daya Bay experiment using three GEANT4 hadronic physics lists—FTFP_BERT_HP, QGSP_BERT_HP, and QGSP_BIC_HP—and develop an innovative methodology for adjusting interaction cross sections based on TALYS nuclear data. The discrepancies between the Daya Bay measurements and the simulations are quantified by comparing both the neutron yield and the tagged neutron multiplicity distributions. The key findings are summarized as follows.

- Differences exist among the various GEANT4 physics lists in their predictions of muon-

induced spallation neutron yields, underscoring the significant model dependency in related background simulations. For cosmic muons with an average energy of ~ 64 GeV, where secondary particles predominantly reside in the sub-GeV kinetic energy regime, the final neutron yield is primarily governed by the choice of the low-energy intranuclear cascade model—either BERT or BIC—rather than by the high-energy string models (FTF or QGS). This work provides a detailed investigation of the impact of the BERT and BIC models on cosmogenic neutron production. A comparison with experimental data reveals that the BIC model yields predictions more consistent with the measurements than the BERT model.

- Rescaling the exclusive inelastic cross sections for neutrons, protons, and gamma rays using TALYS–GEANT4 ratios systematically improves the agreement of the total neutron yield, Y_n , with the experimental data. For the BERT-based models, the discrepancy with the Daya Bay measurement is reduced from approximately 20% to about 6%, while for the BIC-based models it is further reduced from roughly 13% to the sub-percent level ($\sim 0.3\%$). However, it should be noted that the hadronic interaction cross sections provided by TALYS are limited to energies up to 200 MeV and therefore do not extend to the higher-energy regime relevant for the full spallation neutron yield. For future studies, the inclusion of additional nuclear data at higher energies will be essential to further constrain the hadronic interaction models.
- An analysis of the neutron multiplicity distributions reveals that the most significant discrepancy between the experimental data and our simulations persists for single-tagged-neutron events ($N_{\text{multi}} = 1$). This deficit was already identified in a previous comparison that employed GEANT4 (version 9.2p01). A quantitative χ^2 test further demonstrates that predictions from the BIC-based models show better overall agreement with the data.
- Compared to the improvement achieved in the neutron yield with the TALYS-based correction, the adjustment has a differential impact on the tagged neutron multiplicity distributions. While the agreement for multi-neutron events ($N_{\text{multi}} > 1$) improves, a persistent deficit in the yield of single-neutron events remains. Consequently, when single-neutron events are included, the overall χ^2/ndf deteriorates. This indicates that while the TALYS-based correction successfully addresses normalization issues stemming from exclusive cross sections, it unveils a residual discrepancy in the final-state modeling, particularly for channels leading to a single final-state neutron.
- For events with $N_{\text{multi}} = 1$, neutron production is predominantly due to the $\gamma-^{12}\text{C}$ reaction. The relative contribution of this channel is higher in the original BIC-based models than in the BERT-based models or their TALYS-corrected counterparts. Given the superior agreement of the original BIC-based GEANT4 model with the data, a promising strategy for reducing the remaining data–MC discrepancy is to increase the inelastic cross section for the $\gamma-^{12}\text{C}$ channel. Conversely, the persistent deficit in simulated single-neutron events indicates that current implementations of the Fermi break-up and evaporation models in GEANT4 require further refinement to accurately reproduce the experimental multiplicity distributions.

Building on these key findings, we propose a practical two-step strategy for improving background modeling in large LS detectors (e.g., JUNO). First, apply TALYS-based cross section adjustments to obtain an accurate normalization of the total cosmogenic neutron yield for background subtraction. Second, use the residual discrepancies in the neutron multiplicity distributions—particularly the deficit in the $N_{\text{multi}} = 1$ channel—as constraints for the future refinement of intranuclear cascade and deexcitation models. Note that the proposed strategy is applicable not only to LS detectors but also to other large-volume neutrino detectors—such as water Cherenkov detectors (e.g., Hyper-Kamiokande [38]) and liquid-argon time-projection chambers (e.g., DUNE [39])—where accurate modeling of cosmogenic neutron backgrounds is equally critical.

This study establishes a reproducible framework for modeling spallation neutrons and provides a clear strategy for mitigating persistent data–simulation discrepancies. This is achieved through channel-specific cross-section reweighting and targeted parameter scans of intranuclear cascade models. The developed methodology offers a template for the data-driven refinement of hadronic interaction models. Its potential applications extend beyond cosmogenic neutrons to analogous background challenges, such as those posed by atmospheric neutrino neutral-current (NC) interactions [40–44]. Notably, the energy range for cosmogenic neutron production examined in this work encompasses that of the final-state particles generated in such NC interactions.

Acknowledgements

The authors would like to thank Yufeng Li for carefully reading the manuscript and useful comments. This work is supported in part by National Natural Science Foundation of China under Grant Nos. 12405125, 12575210, by the National Key R&D Program of China under Grant No. 2024YFE0110500.

References

- [1] Y. F. Wang, V. Balic, G. Gratta, A. Fasso, S. Roesler and A. Ferrari, “Predicting neutron production from cosmic ray muons,” *Phys. Rev. D* **64** (2001), 013012
- [2] V. A. Kudryavtsev, N. J. C. Spooner and J. E. McMillan, “Simulations of muon induced neutron flux at large depths underground,” *Nucl. Instrum. Meth. A* **505** (2003), 688-698
- [3] T. Hagner, R. von Hentig, B. Heisinger, L. Oberauer, S. Schönert, F. von Feilitzsch and E. Nolte, “Production of cosmogenic isotopes in underground experiments,” *Astropart. Phys.* **14**, 33 (2000)
- [4] S. Abe *et al.* [KamLAND Collaboration], “Production of radioactive isotopes through cosmic muon spallation in KamLAND,” *Phys. Rev. C* **81**, 025807 (2010)
- [5] G. Bellini *et al.* [Borexino Collaboration], “Cosmogenic backgrounds in Borexino at 3800 m w.e.,” *JCAP* **08**, 049 (2013)
- [6] F. P. An *et al.* [Daya Bay Collaboration], “Cosmogenic neutron production at Daya Bay,” *Phys. Rev. D* **97**, 052009 (2018)
- [7] M. Aglietta, G. Badino, G. Bologna, C. Castagnoli, A. Castellina, W. Fulgione, P. Galeotti, O. Saavedra, G. Trinchero, S. Vernetto *et al.*, “Neutron flux generated by cosmic-ray mouns at 5200 hg/cm² sr underground. Depth-neutron intensity curve,” *Il Nuovo Cimento C*, vol. 12, no. 4, pp. 467–477, 1989, Springer.
- [8] R. Hertenberger, M. Chen, B. L. Dougherty, “Muon-induced neutron and pion production in an organic liquid scintillator at a shallow depth,” *Physical Review C*, vol. 52, no. 6, p. 3449, 1995, APS.
- [9] F. Boehm, J. Busenitz, B. Cook, G. Gratta, H. Henrikson, J. Kornis, D. Lawrence, K. B. Lee, K. McKinny, L. Miller *et al.*, “Neutron production by cosmic-ray muons at shallow depth,” *Physical Review D*, vol. 62, no. 9, p. 092005, 2000.
- [10] S. C. Blyth, Y. L. Chan, X. C. Chen, M. C. Chu, K. X. Cui, R. L. Hahn, T. H. Ho, Y. K. Hor, Y. B. Hsiung, B. Z. Hu *et al.*, “Measurement of cosmic-ray muons and muon-induced neutrons in the Aberdeen Tunnel Underground Laboratory,” *Physical Review D*, vol. 93, no. 7, p. 072005, 2016.
- [11] H. M. Araújo, J. Blockley, C. Bungau, M. J. Carson, H. Chagani, E. Daw, B. Edwards, C. Ghag, E. V. Korolkova, V. A. Kudryavtsev *et al.*, “Measurements of neutrons produced by high-energy muons at the Boulby Underground Laboratory,” *Astroparticle Physics*, vol. 29, no. 6, pp. 471–481, 2008.
- [12] L. Reichhart, A. Lindote, D. Yu. Akimov, H. M. Araújo, E. J. Barnes, V. A. Belov, A. Bewick, A. A. Burenkov, V. Chepel, A. Currie *et al.*, “Measurement and simulation of the muon-induced neutron yield in lead,” *Astroparticle Physics*, vol. 47, pp. 67–76, 2013.

- [13] H. M. Araujo *et al.*, “Measurements of neutrons produced by high-energy muons at the Boulby Underground Laboratory,” *Astropart. Phys.* **29**, 471 (2008)
- [14] G. Bellini *et al.* [Borexino Collaboration], “Cosmogenic backgrounds in Borexino at 3800 m water-equivalent depth,” *JCAP* **08**, 049 (2013)
- [15] J. Q. Meindl, “Reconstruction and Measurement of Cosmogenic Signals in the Neutrino Experiment Borexino,” Ph.D. thesis, Technische Universität München (2013)
- [16] K. Abe *et al.* [T2K Collaboration], “First measurement of neutron capture multiplicity in neutrino-oxygen neutral-current quasi-elastic-like interactions using an accelerator neutrino beam,” arXiv:2505.22547 [hep-ex] (2025)
- [17] FLUKA Collaboration, “FLUKA – The official CERN FLUKA website,” <https://fluka.cern/>
- [18] Geant4 Collaboration, “Geant4 – Official website,” <https://geant4.web.cern.ch/>
- [19] A. Abusleme *et al.* [JUNO], “JUNO physics and detector,” *Prog. Part. Nucl. Phys.* **123** (2022), 103927
- [20] A. Koning, S. Hilaire and S. Goriely, “TALYS: modeling of nuclear reactions,” *Eur. Phys. J. A* **59** (2023) no.6, 131
- [21] P. Žugec *et al.*, “Integral measurement of the $^{12}\text{C}(n, p)^{12}\text{B}$ reaction up to 10 GeV,” *European Physical Journal A*, vol. 52, article no. 101, 2016.
- [22] M. Guan, M. C. Chu, J. Cao, K. B. Luk and C. Yang, “A parametrization of the cosmic-ray muon flux at sea-level,” [arXiv:1509.06176 [hep-ex]].
- [23] T. K. Gaisser, R. Engel, and E. Resconi, *Cosmic Rays and Particle Physics*, Cambridge University Press (2016).
- [24] S. Eidelman *et al.* [Particle Data Group], “Review of Particle Physics,” *Phys. Lett. B* **592**, 1 (2004).
- [25] H. Jokisch, K. Carstensen, W. D. Dau, H. J. Meyer and O. C. Allkofer, “COSMIC RAY MUON SPECTRUM UP TO 1-TEV AT 75-degrees ZENITH ANGLE,” *Phys. Rev. D* **19** (1979), 1368-1372
- [26] J. Kremer, M. Boezio, M. L. Ambriola, G. Barbiellini, S. Bartalucci, R. Bellotti, D. Bergstrom, U. Bravar, F. Cafagna and P. Carlson, *et al.* “Measurements of ground-level muons at two geomagnetic locations,” *Phys. Rev. Lett.* **83** (1999), 4241-4244
- [27] P. Achard *et al.* [L3], “Measurement of the atmospheric muon spectrum from 20-GeV to 3000-GeV,” *Phys. Lett. B* **598** (2004), 15-32

- [28] B. C. Rastin, “AN ACCURATE MEASUREMENT OF THE SEA LEVEL MUON SPECTRUM WITHIN THE RANGE 4-GEV/C TO 3000-GEV/C,” *J. Phys. G* **10** (1984), 1609-1628
- [29] C. A. Ayre, J. M. Baxendale, C. J. Hume, B. C. Nandi, M. G. Thompson and M. R. Whalley, “Precise Measurement of the Vertical Muon Spectrum in the Range 20-GeV/c-500-GeV/c,” *J. Phys. G* **1** (1975), 584-600
- [30] P. Antonioli, C. Ghetti, E. V. Korolkova, V. A. Kudryavtsev, and G. Sartorelli, “A three-dimensional code for muon propagation through the rock: MUSIC,” *Astropart. Phys.* **7**, 357 (1997), arXiv:hep-ph/9705408 [hep-ph].
- [31] V. A. Kudryavtsev, “Muon simulation codes MUSIC and MUSUN for underground physics,” *Comput. Phys. Commun.* **180**, 339 (2009), arXiv:0810.4635 [physics.comp-ph].
- [32] F. P. An *et al.* [Daya Bay], “Observation of electron-antineutrino disappearance at Daya Bay,” *Phys. Rev. Lett.* **108** (2012), 171803
- [33] F. P. An *et al.* [Daya Bay], “The Detector System of The Daya Bay Reactor Neutrino Experiment,” *Nucl. Instrum. Meth. A* **811** (2016), 133-161
- [34] GEANT4 Collaboration, “GEANT4 Physics List Guide (Release 11.2),” CERN (2024), available at <https://geant4-userdoc.web.cern.ch/UsersGuides/PhysicsListGuide/html/index.html>.
- [35] A. J. Koning and D. Rochman, “Modern Nuclear Data Evaluation with the TALYS Code System,” *Nucl. Data Sheets* **113**, 2841 (2012).
- [36] A. J. Koning, D. Rochman *et al.*, “TENDL-2017: TALYS-based evaluated nuclear data library,” available at https://tendl.web.psi.ch/tendl_2017/tendl2017.html (2017).
- [37] J. Cheng, X. J. Luo, G. S. Li, Y. F. Li, Z. P. Li, H. Q. Lu, L. J. Wen, M. Wurm and Y. Y. Zhang, “Pulse shape discrimination technique for diffuse supernova neutrino background search with JUNO,” *Eur. Phys. J. C* **84** (2024) no.5, 482
- [38] K. Abe *et al.* [Hyper-Kamiokande], “Hyper-Kamiokande Design Report,” [arXiv:1805.04163 [physics.ins-det]].
- [39] B. Abi *et al.* [DUNE], “Long-baseline neutrino oscillation physics potential of the DUNE experiment,” *Eur. Phys. J. C* **80** (2020) no.10, 978
- [40] J. Cheng, Y. F. Li, L. J. Wen and S. Zhou, “Neutral-current background induced by atmospheric neutrinos at large liquid-scintillator detectors: I. model predictions,” *Phys. Rev. D* **103** (2021) no.5, 053001
- [41] J. Cheng, Y. F. Li, H. Q. Lu and L. J. Wen, “Neutral-current background induced by atmospheric neutrinos at large liquid-scintillator detectors. II. Methodology for *insitu* measurements,” *Phys. Rev. D* **103** (2021) no.5, 053002

- [42] J. Cheng, M. Li, Y. F. Li, G. S. Li, H. Q. Lu and L. J. Wen, “Neutral-current background induced by atmospheric neutrinos at large liquid-scintillator detectors: III. Comprehensive prediction for low energy neutrinos,” *Eur. Phys. J. C* **85** (2025) no.3, 295
- [43] S. Han *et al.* [Super-Kamiokande], “Measurement of neutron production in atmospheric neutrino interactions at Super-Kamiokande,” *Phys. Rev. D* **112** (2025) no.1, 012004
- [44] S. Sakai *et al.* [Super-Kamiokande], “Measurement of the neutrino-oxygen neutral-current quasielastic cross section using atmospheric neutrinos in the SK-Gd experiment,” *Phys. Rev. D* **109** (2024) no.1, L011101